























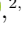



## TEMPLATES: Characterization of a Merger in the Dusty Lensing SPT0418-47 System

JARED CATHEY <sup>1</sup>, ANTHONY H. GONZALEZ <sup>1</sup>, SIDNEY LOWER <sup>1</sup>, KEDAR A. PHADKE <sup>2,3</sup>, JUSTIN SPILKER <sup>4</sup>,  
MANUEL ARAVENA <sup>5</sup>, MATTHEW BAYLISS <sup>6</sup>, JACK E. BIRKIN <sup>4</sup>, SIMON BIRRER <sup>7</sup>, SCOTT CHAPMAN <sup>8,9,10,11</sup>,  
HÅKON DAHLE <sup>12</sup>, CHRISTOPHER C. HAYWARD <sup>13</sup>, YASHAR HEZAVEH <sup>13,14,15,16</sup>, RYLEY HILL,<sup>10</sup>  
TAYLOR A. HUTCHISON <sup>17</sup>, KEUNHO J. KIM <sup>6</sup>, GUILLAUME MAHLER <sup>18,19</sup>, DANIEL P. MARRONE <sup>20</sup>,  
DESIKA NARAYANAN <sup>21</sup>, ALEXANDER NAVARRE <sup>6</sup>, CASSIE REUTER <sup>2</sup>, JANE R. RIGBY <sup>22</sup>, KEREN SHARON <sup>23</sup>,  
MANUEL SOLIMANO <sup>24</sup>, NIKOLAUS SULZENAUER <sup>25</sup>, JOAQUIN VIEIRA <sup>2,26,3</sup> AND DAVID VIZGAN <sup>2</sup>

<sup>1</sup>*Department of Astronomy, University of Florida, 211 Bryant Space Sciences Center, Gainesville, FL 32611 USA*

<sup>2</sup>*Department of Astronomy, University of Illinois, 1002 West Green St., Urbana, IL 61801, USA*

<sup>3</sup>*Center for Astrophysical Surveys, National Center for Supercomputing Applications, 1205 West Clark Street, Urbana, IL 61801, USA*

<sup>4</sup>*Department of Physics and Astronomy and George P. and Cynthia Woods Mitchell Institute for Fundamental Physics and Astronomy, Texas A&M University, 4242 TAMU, College Station, TX 77843-4242, USA*

<sup>5</sup>*Núcleo de Astronomía, Facultad de Ingeniería y Ciencias, Universidad Diego Portales, Av. Ejército 441, Santiago, Chile*

<sup>6</sup>*Department of Physics, University of Cincinnati, Cincinnati, OH 45221, USA*

<sup>7</sup>*Department of Physics and Astronomy, Stony Brook University, Stony Brook, NY 11794, USA*

<sup>8</sup>*Department of Physics and Atmospheric Science, Dalhousie University, Halifax, NS, B3H 4R2, Canada*

<sup>9</sup>*NRC Herzberg Astronomy and Astrophysics, 5071 West Saanich Rd, Victoria, BC, V9E 2E7, Canada*

<sup>10</sup>*Department of Physics and Astronomy, University of British Columbia, Vancouver, BC, V6T1Z1, Canada*

<sup>11</sup>*Eureka Scientific Inc, Oakland, CA 94602, USA*

<sup>12</sup>*Institute of Theoretical Astrophysics, University of Oslo, P.O. Box 1029, Blindern, NO-0315 Oslo, Norway*

<sup>13</sup>*Center for Computational Astrophysics, Flatiron Institute, 162 5th Avenue, 10010, New York, NY, USA*

<sup>14</sup>*Department of Physics, Université de Montréal, Montréal, Canada*

<sup>15</sup>*Ciela - Montreal Institute for Astrophysical Data Analysis and Machine Learning, Montréal, Canada*

<sup>16</sup>*Mila - Quebec Artificial Intelligence Institute, Montréal, Canada*

<sup>17</sup>*Observational Cosmology Lab, Code 665, NASA Goddard Space Flight Center, 8800 Greenbelt Rd., Greenbelt, MD 20771, USA\**

<sup>18</sup>*Centre for Extragalactic Astronomy, Durham University, South Road, Durham DH1 3LE, UK*

<sup>19</sup>*Institute for Computational Cosmology, Durham University, South Road, Durham DH1 3LE, UK*

<sup>20</sup>*Steward Observatory, University of Arizona, 933 North Cherry Avenue, Tucson, AZ 85721, USA*

<sup>21</sup>*Department of Astronomy, University of Florida, Gainesville, FL USA 32611-2055*

<sup>22</sup>*Observational Cosmology Lab, Code 665, NASA Goddard Space Flight Center, Greenbelt, MD 20771*

<sup>23</sup>*University of Michigan, Department of Astronomy, 1085 South University Avenue, Ann Arbor, MI 48109, USA*

<sup>24</sup>*Instituto de Estudios Astrofísicos, Facultad de Ingeniería y Ciencias, Universidad Diego Portales, Avenida Ejército Libertador 441, Santiago, Chile. [Código Postal 8370191]*

<sup>25</sup>*Max-Planck-Institut für Radioastronomie, Auf dem Hügel 69, 53121 Bonn, Germany*

<sup>26</sup>*Department of Physics, University of Illinois, 1110 West Green St., Urbana, IL 61801, USA*

### ABSTRACT

We present JWST and ALMA results for the lensing system SPT0418–47, which includes a strongly-lensed, dusty star-forming galaxy at redshift  $z = 4.225$  and an associated multiply-imaged companion. JWST NIRC<sub>am</sub> and MIRI imaging observations presented in this paper were acquired as part of the Early Release Science program Targeting Extremely Magnified Panchromatic Lensed Arcs and Their Extended Star Formation (TEMPLATES). This data set provides robust, multiwavelength detection of stellar light in both the main (SPT0418A) and companion (SPT0418B) galaxies, while the ALMA detection of [C II] emission confirms that SPT0418B lies at the same redshift as SPT0418A. From a source plane reconstruction, we infer that the projected physical separation of the two galaxies is  $4.42 \pm 0.05$  kpc. We derive total magnifications of  $\mu = 29.5 \pm 1.2$  and  $\mu = 4.2 \pm 0.9$  for SPT0418A and

Corresponding author: Jared Cathey

jaredcathey@ufl.edu

SPT0418B, respectively. We use both CIGALE and PROSPECTOR to derive stellar masses. The stellar mass ratio of SPT0418A and SPT0418B is approximately 4 to 1 ( $4.5 \pm 1.0$  for CIGALE and  $4.2_{-1.6}^{+1.9}$  for PROSPECTOR). We also see evidence of extended structure associated with SPT0418A in the lensing reconstruction that is suggestive of a tidal feature. Interestingly, the star formation rates and stellar masses of both galaxies are consistent with the main sequence of star-forming galaxies at this epoch, indicating that this ongoing interaction has not noticeably elevated the star formation levels.

*Keywords:* High redshift galaxies (734)

## 1. INTRODUCTION

In the standard paradigm of galaxy formation, present-day spiral galaxies are products of hierarchical assembly, with the disks arising after the last major merger either as a byproduct of dissipative mergers (e.g. Robertson et al. 2006; Governato et al. 2009) or from subsequent gas accretion and minor dissipative mergers (e.g. Baugh et al. 1996; Steinmetz & Navarro 2002). In this picture, dynamically cold disks become increasingly rare at higher redshifts (e.g. Hopkins et al. 2010). Disks are expected to be highly turbulent and clumpy, driving significant outflows, and the ratio of rotational velocity to turbulent velocity,  $V/\sigma$ , should decrease with increasing redshift (Pillepich et al. 2019). Moreover, mergers can induce bursts of star formation, and hence can drive star formation at early times when mergers are expected to be more frequent (Sanders et al. 1988; Hopkins et al. 2008; Sotillo-Ramos et al. 2022). Studies of high-redshift submillimeter galaxies (SMGs) have supported a picture in which many of these strongly star-forming galaxies are major mergers (Engel et al. 2010; Alaghband-Zadeh et al. 2012; Marrone et al. 2018; Litke et al. 2019; Perry et al. 2022).

A counterpoint to this picture was presented by Rizzo et al. (2020), who found that the dusty, strongly star-forming galaxy SPT0418–47 at  $z = 4.225$  exhibits orderly disk rotation with  $V/\sigma = 9.7 \pm 0.4$  for the gas, based upon observations from the Atacama Large Millimeter Array (ALMA). This ratio is a factor of  $\sim 3$  higher than predicted at this epoch (Pillepich et al. 2019), and the lack of dynamical signatures of a merger argued that the high star formation rate is driven purely by internal processes. Using ALMA, Roman-Oliveira et al. (2023) have more recently found additional regularly rotating disks at  $z \sim 4.5$ , and Nelson et al. (2022) have uncovered with the James Webb Space Telescope (JWST) a population of massive, dusty disks at  $z = 2 - 6$ .

In this paper we re-examine SPT0418–47 using JWST imaging and new ALMA observations. SPT0418–47 is one of four targets of the JWST Early Release Science (ERS) program Targeting Extremely Magnified Panchromatic Lensed Arcs and their Extended Star formation (TEMPLATES, ERS Program 1355, PI: Rigby ; Co-PI: Vieira). The overall aim of TEMPLATES is to use multiple tracers to study the spatially-resolved star formation in four strongly lensed galaxies spanning a range of redshift and star formation rates. SPT0418–47 has the highest redshift of these four targets.

Originally discovered as a submillimeter source by the South Pole Telescope (Vieira et al. 2013), SPT0418–47 is known to have a high star formation rate ( $\sim 280 M_{\odot} \text{ yr}^{-1}$ ) with a dense, solar-metallicity interstellar medium (ISM) from observations with the Atacama Pathfinder EXperiment (APEX) and ALMA (De Breuck et al. 2019). Spilker et al. (2020) also observed an outflow of molecular gas in this galaxy with  $\dot{M} \sim 150 M_{\odot} \text{ yr}^{-1}$ .

In this paper, we use NIRCcam (Rieke, M., Kelly, D. M., Misselt, K., et al. 2023, submitted to PASP) and MIRI (Wright, G., Rieke, G. H., Glasse, A., et al. 2023, submitted to PASP) imaging to spatially resolve stellar emission in this system.

We combine JWST imaging and ALMA [C II] data and investigate the environment of this system to discern whether this system is isolated or is dynamically interacting. As part of this analysis, we perform lens modeling to reconstruct the source plane image of SPT0418–47.

We describe the data in §2. In §3 we describe the nearby companion, which was also reported by Peng et al. (2022). Hereafter we designate the companion SPT0418B and the main galaxy SPT0418A. Next, in §4 we discuss the lens modeling, dynamical state of the system, conduct Spectral Energy Distribution (SED) modeling, and estimate the stellar mass. In §5 we have our concluding remarks. Throughout we assume a Planck cosmology (Planck Collaboration et al. 2020):  $H_0 = (67.4 \pm 0.5) \text{ km s}^{-1} \text{ Mpc}^{-1}$ ,  $\Omega_m = 0.315 \pm 0.007$ ,  $\Omega_{\Lambda} = 0.685 \pm 0.007$ .

\* NASA Postdoctoral Fellow

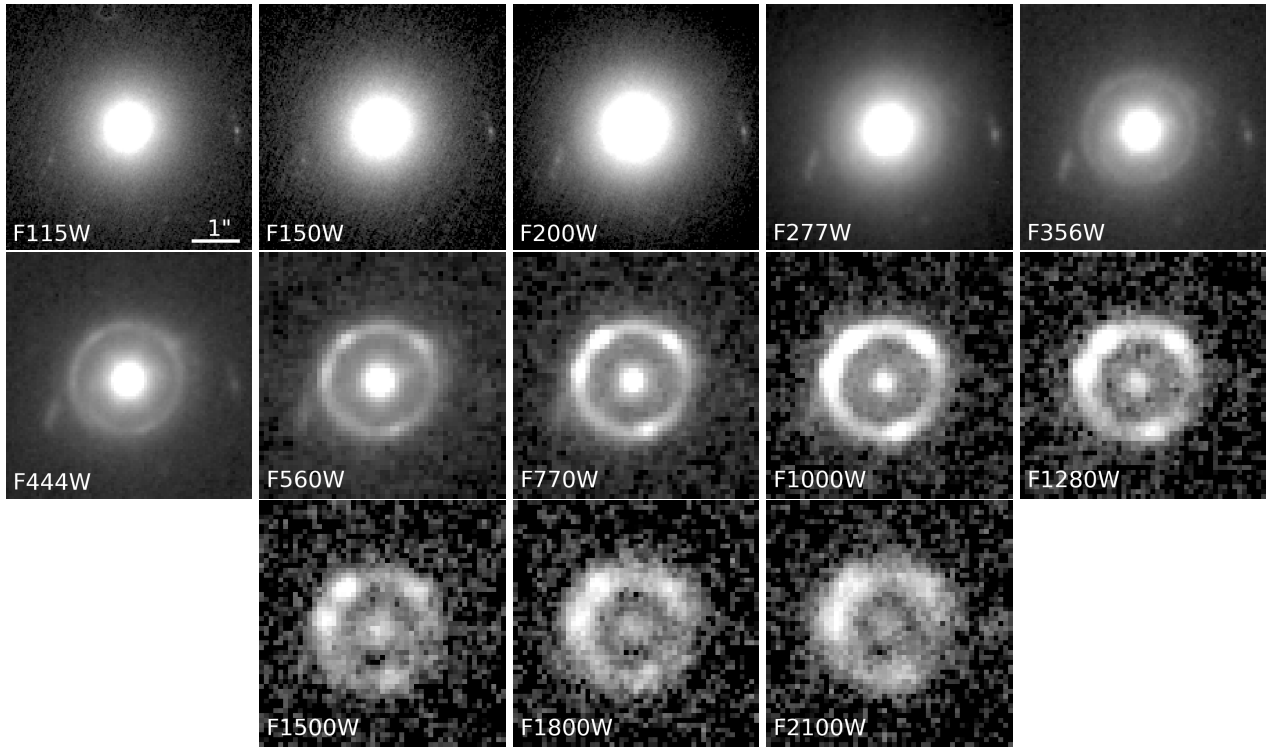


**Figure 1.** Images of SPT0418–47 in all 13 NIRCcam and MIRI passbands ranging from  $1.15\mu\text{m}$  –  $21\mu\text{m}$ . These images illustrate the contrast as a function of wavelength between the foreground lens, SPT0418A, and SPT0418B. Specific locations of SPT0418B are shown in Figure 2. The images are displayed with square-root scaling. The minimum value of the flux density scale is set to  $0.1\text{ MJy/sr}$  below sky; the maximum in each frame is  $2\text{ MJy/sr}$  above the sky level. A  $1''$  scale bar is included in the upper left panel.

## 2. DATA AND PROCESSING

### 2.1. JWST

Instruments on board JWST have been shown to be working well, and in some cases performing better than expected (Rigby et al. 2023). Imaging observations of SPT0418–47 were taken by the NIRCcam and MIRI instruments on 2022 August 11 and 2022 August 22, respectively, as part of the TEMPLATES program. Imaging was taken with filters spanning wavelengths from  $1.15\mu\text{m}$  to  $21\mu\text{m}$ , with the target centered in detector B4 for NIRCcam. The filters and corresponding exposure times are given in the Appendix in Table 3.

Rigby et al. 2023 (in prep) describes in detail the data reduction process for TEMPLATES. Here we summarize the process for the subset of TEMPLATES data analyzed in this paper. Starting with the Level 2A data products for NIRCcam, we applied a custom de-stripping algorithm to correct for  $1/f$  noise and jumps between amplifiers. The de-stripped images were then run through the JWST pipeline (Version 1.8.2) using the CRDS context  `JWST_0988.pmap`.

This version of the official JWST calibration was the most up-to-date at the time of this analysis, and is con-

sistent to within 3% of the absolute flux calibration in Boyer et al. (2022).

For the MIRI imaging, we used a four-point dither pattern optimized for extended sources. Uncalibrated images were processed through the JWST pipeline version 1.9.5dev using `pmap JWST_1062.pmap`. There are known striping issues for MIRI imaging, mainly arising from detector  $1/f$  noise. We implemented de-stripping for the current data by creating a detector template using the four dither positions and removing it from each exposure after stage 2 of the pipeline.<sup>1</sup> These de-stripped stage 2 data products were processed through the stage 3 pipeline, and the images output from stage 3 were used for the analysis in this paper.

We realigned the MIRI and NIRCcam imaging to a common frame to correct for residual astrometric offsets, and generated a simulated point spread function (PSF) for each filter for the date of observation using WebbPSF version 1.0.1.dev126+g6d83a9d (Perrin et al. 2012, 2014) given the measured wavefront of the telescope, which is measured every 2 days (McElwain et al.

<sup>1</sup> [https://github.com/STScI-MIRI/Imaging\\_ExampleNB/blob/main/helpers/miri\\_clean.py](https://github.com/STScI-MIRI/Imaging_ExampleNB/blob/main/helpers/miri_clean.py)

2023). Cutouts of SPT0418–47 in the F115W through F2100W filters are shown in Figure 1, illustrating the relative contrast between the lensing galaxy and the SPT0418–47 system as a function of wavelength.

## 2.2. ALMA

We combine ALMA observations of the [C II] 158  $\mu\text{m}$  line and underlying dust continuum observed in projects 2016.1.01374.S (PI: Hezaveh) and 2016.1.01499.S (PI: Litke). Both projects used a similar correlator setup, centering the [C II] line in the upper sideband, while the lower sideband provides continuum data. The total on-source time between both projects was 4.9 hours. We performed a continuum subtraction in the  $uv$  plane assuming a linear frequency dependence of the continuum emission, excluding frequencies with significant [C II] emission from the fit.

Individual observing blocks from each project span a wide range in spatial resolution from  $0.02''$  to  $0.15''$ . We jointly imaged the data (accounting for the different phase centers and frequency setups of the two projects) using `tclean` in the CASA software package (McMullin et al. 2007; THE CASA TEAM et al. 2022), combining all line-free frequency channels to create a continuum image. We also imaged the [C II] line emission using the continuum-subtracted data with a spectral resolution of  $50 \text{ km s}^{-1}$ . We base our analysis on images created applying a  $50 \text{ mas}$  external taper in the  $uv$ -plane, which offers a reasonable compromise between spatial resolution and sensitivity and is well-matched to the resolution of the NIRC*am* imaging. The final synthesized beam size was  $93 \text{ mas} \times 97 \text{ mas}$ , reaching a sensitivity of  $0.20 \text{ mJy/beam}$  in  $50 \text{ km s}^{-1}$  channels of the [C II] cube after correcting for the primary beam response at the position of the lens. We produced integrated and flux-weighted mean velocity maps of the [C II] emission after masking pixels detected at  $< 3\sigma$  significance.

## 3. DETECTION OF THE MULTIPLY-IMAGED COMPANION

There are multiple sources near SPT0418A that could be physically associated if they lie at the same redshift. In this section we investigate each of these sources, then perform a source plane reconstruction of SPT0418–47.

### 3.1. The Multiply-Imaged Companion

The JWST imaging reveals in detail the stellar emission from SPT0418A. To better view SPT0418–47, we model and remove the flux from the foreground lens, which is an elliptical galaxy at  $z = 0.263$ . We use GALFIT (Peng et al. 2002, 2010) to fit a Sérsic bulge to the foreground lens at the wavelength of the F150W

bandpass, convolving the model with the PSF from WebbPSF. In the model we also add a secondary exponential disk component to improve the model in the central region of the galaxy. During the fitting, we mask nearby galaxies and use the error map to weight the fit. The best fit  $\chi^2$  model for the bulge has  $n = 3.17 \pm 0.02$  and  $r_e = 0.88 \pm 0.01''$ , while the disk component has  $r_e = 0.067 \pm 0.001''$  and contains 7% of the total light.

We take the best fit in F150W, fix the axis ratios, position angles of the two components, and Sérsic parameter, and then model the lensing galaxy at the other wavelengths, using the appropriate PSFs from WebbPSF. We allow the position, physical scale, and flux to be free parameters. The position is left free to account for any remaining subpixel astrometric offsets between images, while the physical scale is left free to account for radial color gradients.

In the left panel of Figure 2, we show a 3-color image of the lensed galaxy after removal of the foreground lens.<sup>2</sup> In this image we can now see two bluer objects, one interior to the arc and the other exterior on the opposite side. This geometry is consistent with multiple lensed images of a single companion (SPT0418B), as discussed by Peng et al. (2022). Proximity of the SPT0418A and SPT0418B in the image plane is suggestive of a small separation in the source plane.

The ALMA [C II] data also shows clear emission signatures at the locations of the two images of SPT0418B. In the center panel of Figure 2 we present contours from the ALMA [C II] data, integrated from  $-100$  to  $0 \text{ km s}^{-1}$  relative to the central velocity of SPT0418A, overlaid on the NIRC*am* imaging. This emission confirms that SPT0418B is very close to SPT0418A not only in the image plane, but also in velocity space. Both images of SPT0418B have consistent mean relative velocities of approximately  $-56 \text{ km s}^{-1}$ .

### 3.2. Other Potential Companions

In addition to SPT0418B, there are two more objects visible only in the NIRC*am* filters at small angular separation. These objects, located at  $(04:18:39.4, -47:51:52.81)$  and  $(04:18:39.6, -47:51:54.76)$ , are close enough that they would both have projected physical separations of  $\sim 10 \text{ kpc}$  from SPT0418A if at the same redshift. These objects do not appear in the ALMA [C II] data, and photometric redshift estimates using CIGALE give redshifts of  $z_{\text{phot}} = 0.4 \pm 0.25$  and  $z_{\text{phot}} < 0.05$  for the West and South objects respectively. We thus conclude

<sup>2</sup> We mask the noisy residual at the center of the foreground galaxy in this image.

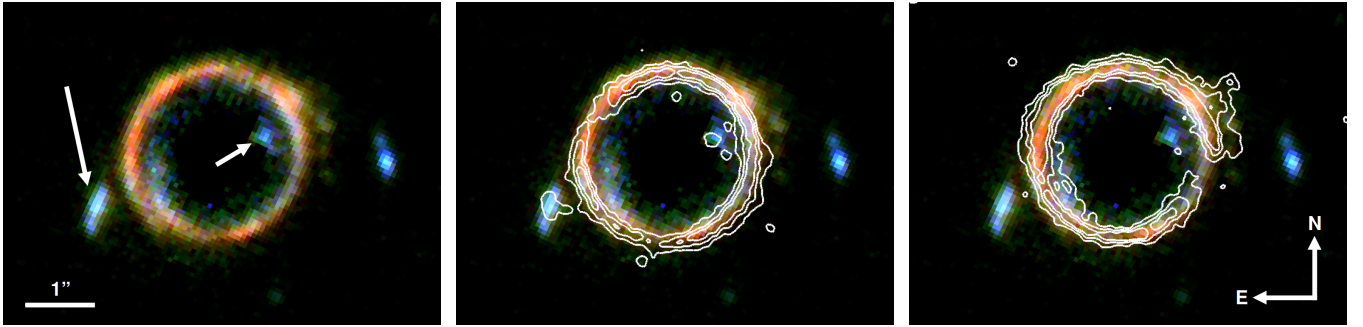


**Figure 2.** Residual color image of SPT0418–47 generated from the F277W, F356W, and F444W NIRCcam imaging after modeling and removal of the foreground lens using GALFIT. The left panel shows SPT0418A and SPT0418B, with arrows denoting the two images of SPT0418B. [C II] contours at the rest frame of SPT0418–47 are overlaid on the NIRCcam image in the center panel integrated over the channels where the companion appears. Slight offsets between the ring and the contours in the center panel are due to the contours being integrated only over the channels where the companion appears most strongly, rather than the whole ring. In the right panel we show the [C II] contours integrated to show the extended feature opposite the companion, connected to the ring formed by the lensing of SPT0418A. The center of the region where the foreground lens was subtracted is masked because the statistical noise is high.

that these objects lie in the foreground and are not associated with SPT0418A or SPT0418B.

#### 4. EVIDENCE FOR AN ONGOING MERGER

Given the projected proximity of SPT0418B, we next explore whether this system is an ongoing merger, and attempt to constrain its physical parameters.

##### 4.1. Source Plane Reconstruction and Kinematics

We perform source plane reconstruction using LENSTRONOMY (Birrer & Amara 2018; Birrer et al. 2021). LENSTRONOMY is capable of joint parametric fitting of the foreground lens mass distribution and flux distribution of the background source, and enables simultaneous fitting of multiple photometric bands. Further, it can use “shapelets” (Birrer et al. 2015; Refregier 2003; Refregier & Bacon 2003; Massey & Refregier 2005), which are a series of 2D basis functions, to rapidly reconstruct the source plane without parametric models of the source light, so long as an accurate lens model is used. As a non-parametric method of source plane reconstruction, shapelets can reconstruct substructures that are missed by simple parametric models. Finally, LENSTRONOMY can add shapelets on top of parametric models of the source to find any additional substructure in the source plane without using many orders of shapelets for structures that are well described by parametric models.<sup>3</sup>

<sup>3</sup> One feature of shapelets is that the final models can include regions with unphysical negative flux values. The presence of negative values is intrinsic to the shapelet approach. In the idealized case the summation of the shapelets should result in a net positive flux at all locations, but when modeling with a limited number of shapelets these unphysical negative flux occur at some locations surrounding bright, positive features.

To model the global structure of the SPT0418–47 system, we start by using elliptical Sérsic profiles. These simple models provide a good first order fit to the profiles. To model the mass profile of the lensing galaxy, we use a Singular Isothermal Ellipsoid (SIE) with external shear. We perform multi-band fitting of our GALFIT-subtracted data in F277W, F356W, F444W, F560W, and F770W. Starting with only the parametric profiles, we first pre-sample the space using a Particle Swarm Optimization (PSO Kennedy & Eberhart 1995) to get near the solution while sampling the high-dimensional space quickly. We then use this approximate solution to seed the Markov Chain Monte Carlo (MCMC) sampler emcee (Foreman-Mackey et al. 2013), allowing it to run to convergence. We then add shapelets to the source model at each wavelength to better model any substructure for each image.

In this lens modeling, due to the prior GALFIT subtraction of the lens light, we found difficulty in modeling both SPT0418A and SPT0418B when including the background noise with LENSTRONOMY. In the future, it would be prudent to perform the lens light subtraction within the software used to conduct the lens modeling rather than using two separate methods. As part of this modeling, we imposed a prior that all values below a threshold of  $0.01\sigma$  less than the median are ignored. This prior forces LENSTRONOMY to consider only flux from regions with higher SNR.

From the source plane reconstruction, we find that the projected physical separation between the centers of the two galaxies is  $4.42 \pm 0.05$  kpc. In modeling the source plane with pure Sérsic profiles, we are unable to reproduce some of the features in both SPT0418A and SPT0418B. By adding shapelets on top of these

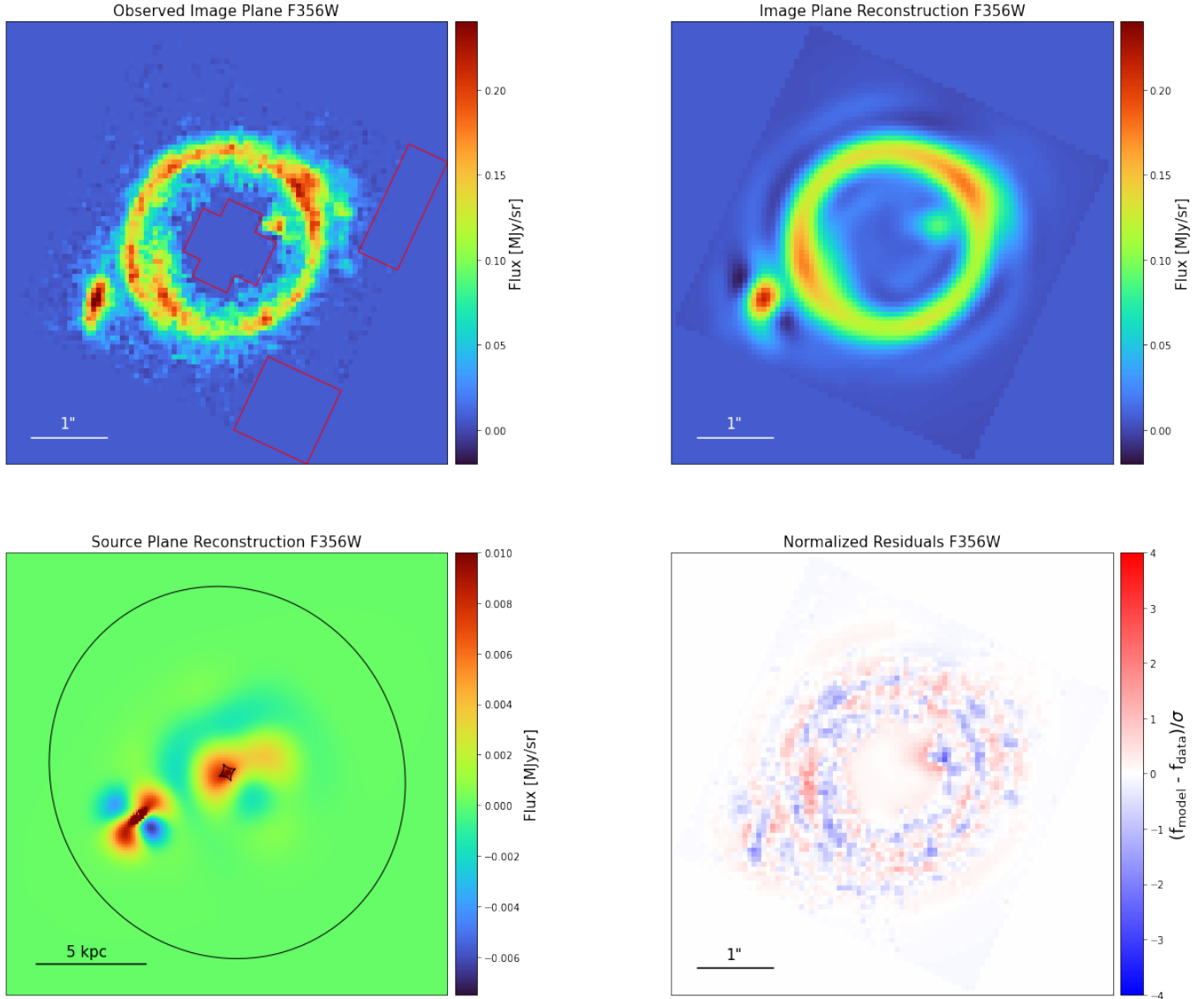


**Figure 3.** Source plane reconstruction of the F356W band. This band is chosen as the flux from the substructure is strongest relative to the peak of the cores for SPT0418A and SPT0418B. The top left panel shows the GALFIT subtracted observed image plane of SPT0418A, with regions masked out due to unassociated flux outlined in red. The top right panel is the reconstructed image plane using a combination of parametric models and shapelets. The bottom left image is a zoomed-in view of the source plane reconstruction with the caustic and critical curve overlaid, while the bottom right panel shows the normalized residuals in the image plane. All panels are rotated such that North is up and East is left.

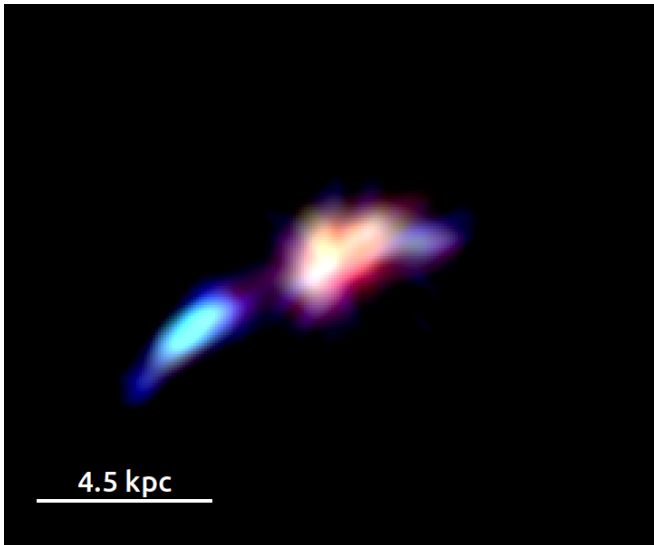
Sérsic profiles, we are able to reproduce those features in the image plane, leading to the reconstruction shown in Figure 3.

Figure 3 shows the lens model in the F356W filter, a band in which both SPT0418B and extended structure associated with SPT0418A can be clearly seen. We list the parameters for the lens model of this system in Table 1 along with estimated uncertainties.

Next, we use the parametric lens mass model listed in Table 1 to generate a backwards ray tracing of the system. This approach provides an alternative to the joint parametric - shapelet fitting shown in Figure 3 for

assessing the presence of additional structures. We take the NIRCAM F277W, F356W, and F444W imaging and map it back to the source plane, accounting for magnifications of the multiple images to create the source plane reconstruction. The result is shown in Figure 4. In this Figure, we again see some extended structure in the light distribution, consistent with that inferred from the shapelets.

Finally, we create a velocity moment map from the [C II] data in Figure 5. Internal gradients are visible in both SPT0418A and SPT0418B. As highlighted by the ellipses in Figure 5, the velocity gradients for the two



**Figure 4.** We show a source plane reconstruction generated using backward ray tracing. We produce this reconstruction using the F277W, F356W, and F444W filters as in Figure 2. The dust-obscured galaxy SPT0418A is on the right, and the bluer SPT0418B is on the left.

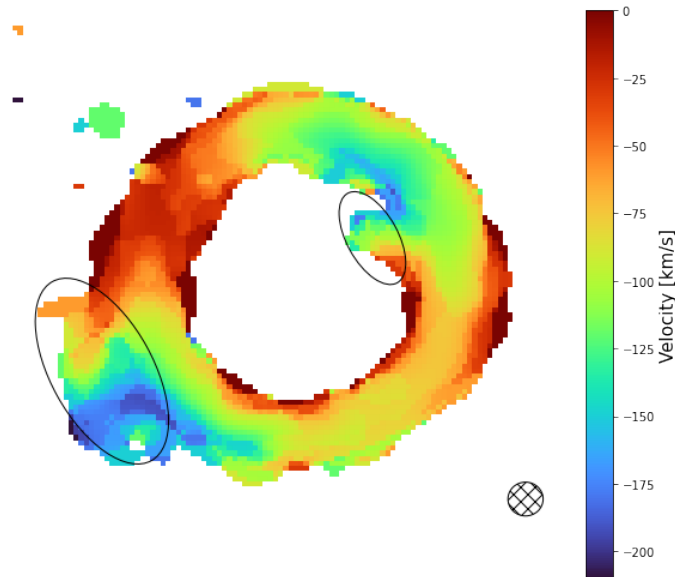


**Figure 5.** ALMA velocity map of the SPT0418–47 system, scaled to highlight the internal velocity gradient of SPT0418B. The two ellipses are the regions where emission from SPT0418B is expected, and the area within these two ellipses show mirrored velocity gradients as expected from the lensing geometry. In the bottom right we show the beam size as the cross-hatched ellipse.

images of SPT0418B are equal and mirrored, as must be true if we are observing multiple images of the galaxy.

#### 4.2. Stellar Mass Ratios

**Table 1.** Lens Model Parameters

Parameter	Model Value <sup>a</sup>
$\theta_E$	$1.207 \pm 0.002$
$\epsilon_1$	$-0.031 \pm 0.006$
$\epsilon_2$	$0.061 \pm 0.009$
$x_{\text{Lens}}$	$-0.010 \pm 0.003$
$y_{\text{Lens}}$	$-0.003 \pm 0.002$
$\gamma_1$	$-0.005 \pm 0.003$
$\gamma_2$	$-0.007 \pm 0.004$

<sup>a</sup>Uncertainties are estimated taking the average of the 16th and 84th percentiles from the marginalized distributions of the MCMC. LENSSTRONOMY parameters are defined as follows:  $\theta_E$  is the circularized Einstein Radius,  $\epsilon_1$  and  $\epsilon_2$  are the x and y components to the ellipticity,  $x_{\text{Lens}}$  and  $y_{\text{Lens}}$  are the offset from the center of the image in arcseconds, and  $\gamma_1$  and  $\gamma_2$  are the external shear components. The orientation of this model is in the native imaging plane, with rotations introduced afterwards as to not introduce autocorrelation noise. The rotation is 245 degrees clockwise from North up and East left.

We next compare the stellar masses of the two components. We use the lens model from above (Table 1) to derive the magnifications of SPT0418A and SPT0418B. We find total magnifications of  $\mu = 29 \pm 1$  for SPT0418A and  $\mu = 4.2 \pm 0.9$  for SPT0418B. The uncertainties on the magnifications are derived from 100 random draws of the MCMC, calculating the flux in the image and the source plane reconstructions of the parametric model. The multiple images of SPT0418B have effective magnifications of  $\mu = 1.2 \pm 0.3$  and  $\mu = 2.9 \pm 0.6$  for the inner and outer image, respectively. For SPT0418B we use only the data for the source exterior to the SPT0418A ring to minimize photometric uncertainties due to overlap with the ring.

To compare the stellar masses of SPT0418A and SPT0418B, we extract the photometry for each using fixed photometric apertures. Figure 6 shows the apertures used for each component. These apertures are designed to be large enough that there is minimal differential flux loss due to the wavelength dependence of the PSF. The flux densities derived for each source are presented in the appendix in Table 3. Reuter et al. (2020) also provides 100  $\mu\text{m}$  – 3 mm SPT, LABOCA, Herschel/SPIRE, ALMA, and Herschel/PACS data for SPT0418–47. These flux densities include contributions from both SPT0418A and SPT0418B. From the ALMA

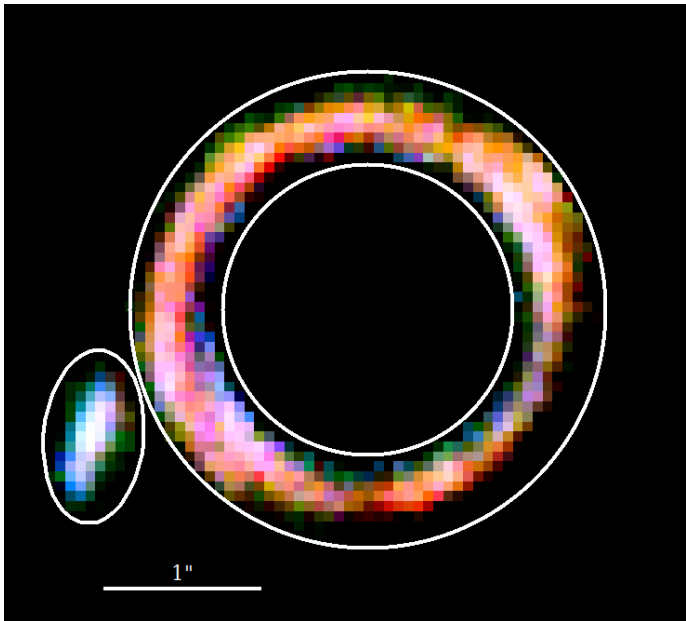


**Figure 6.** Apertures used for SPT0418A and SPT0418B galaxy. The inner image of SPT0418B was not used to extract photometry because it is more sensitive to residuals from the subtraction of the lensing galaxy than the outer image.

data, we measure that  $96 \pm 2\%$  of the flux is associated with SPT0418A. When fitting the SED for SPT0418A, we include this fraction of the flux density for all bands measured by Reuter et al. (2020). The differences in SFR and stellar mass between using this fractional flux and the total flux are smaller than the statistical uncertainties.

We use both CIGALE (Boquien et al. 2019) and PROSPECTOR (Johnson et al. 2021) to fit the SEDs. This provides a measure of systematic uncertainties associated with assumptions in the SED modeling. For both codes we assume a Chabrier IMF (Chabrier 2003). For both codes we use a flexible attenuation curve parameterization that allows for a variable UV-optical slope and V-band attenuation: Specifically, CIGALE uses the parameterization from Boquien et al. (2019) and PROSPECTOR that of Kriek & Conroy (2013). The metallicity is allowed to vary for SPT0418A, and we apply a prior that the metallicity must be between 80% and 125% of solar, consistent with De Breuck et al. (2019), Peng et al. (2022), and our team’s in-progress spectroscopic analysis (Birkin et al., submitted).

For SPT0418B, we set a uniform prior between 65–75% solar on the metallicity for PROSPECTOR based upon the NIRSpc analysis of Birkin et al. (in prep). We fix the metallicity to solar for CIGALE, as this is the clos-

est metallicity value available in the code. With CIGALE, we model the SFH parametrically as an exponential decay ( $\tau_{\text{best}} = 1$  Gyr) with an additional burst component using the Bruzual & Charlot (2003) stellar population model. In contrast, PROSPECTOR uses Flexible Stellar Population Synthesis (FSPS) stellar population modeling (Conroy et al. 2009; Conroy & Gunn 2010) and we allow a non-parametric SFH with a Dirichlet prior on the mass formed per time bin (Leja et al. 2019). Lower et al. (2020) demonstrated with simulations that such an approach can outperform parametric models. The PROSPECTOR fit also permits a non-uniform dust screen, and we let the fractional obscuration be a free parameter (Lower et al. 2022). The posterior for the obscured fraction peaks at  $> 98\%$  for SPT0418A; however, the small amount of light that is unobscured is important in the SED fit.

In Figure 7 we show the SED models that best fit our data with each code for both SPT0418A and SPT0418B. Similarly, the derived quantities from these SED Models are presented in Table 2. The constraints on SPT0418B are less robust due to the more limited set of photometric detections since this source is relatively faint and the MIRI integration times are short. For PROSPECTOR, we plot the median and  $1\sigma$  spread in the model SEDs, and for CIGALE we plot the model corresponding to the minimum  $\chi^2$ .<sup>4</sup> For PROSPECTOR, we find that it fits the FIR dust emission poorly. Thus, we had PROSPECTOR model only the stellar emission of the SED as to not have the improper dust models bias the fit. The reduced  $\chi^2$  statistics for the CIGALE fits to the SPT0418A and SPT0418B SEDs are 3.35 and 0.48, respectively, and 3.42 and 0.54 when fit with PROSPECTOR. The differences in  $\chi^2$  values between the two sources are caused by both number of observations and models. Since SPT0418B only has one data point in the FIR, it overfits the point for all of the FIR emission.<sup>5</sup>

A comparison of the results from the two SED modeling codes in Table 2 shows that the derived star formation rates and effective  $A_V$  from CIGALE and PROSPECTOR are consistent within the uncertainties for both SPT0418A and SPT0418B. The inferred stellar metallicity for the main source is consistent with the solar value we have assumed in the CIGALE model.

The most significant discrepancy between the two codes is with the inferred stellar mass. For SPT0418A, CIGALE infers a magnification-corrected stellar mass of

<sup>4</sup> CIGALE does not calculate the  $1\sigma$  spread in model SEDs.

<sup>5</sup> We note that the  $\chi^2$  values for the two SED fitting packages are not directly comparable because the codes use different methodologies to find the best fit SEDs.



**Table 2.** SED Modeling Results

Source	Magnification $\mu$	Code	Stellar Mass ( $\mu M_{\odot}$ )	SFR <sub>100</sub> ( $\mu M_{\odot}/\text{yr}$ )	$Z_*$ ( $Z_{\odot}$ )	$A_V$	sSFR ( $10^{-9} M_{\odot} \text{ yr}^{-1}$ )
SPT0418A	$29.5 \pm 1.2$	PROSPECTOR	$10.2^{+3.4}_{-1.9} \times 10^{11}$	$4257^{+989}_{-742}$	$0.94^{+0.15}_{-0.11}$	$3.75^{+0.12}_{-0.14}$	$4.2^{+1.0}_{-0.7}$
		CIGALE	$4.5 \pm 0.9 \times 10^{11}$	$3770 \pm 545$	1	$3.8 \pm 0.1$	$8.4 \pm 1.2$
SPT0418B	$2.92 \pm 0.63$	PROSPECTOR	$23.9^{+9.1}_{-7.2} \times 10^9$	$25.3^{+23.6}_{-15.2}$	$0.68^{+0.04}_{-0.02}$	$1.5^{+0.32}_{-0.43}$	$1.1^{+1.1}_{-0.7}$
		CIGALE	$9.8 \pm 0.5 \times 10^9$	$43.6 \pm 17.9$	1	$1.4 \pm 0.2$	$4.4 \pm 1.8$

NOTE—Quoted parameter results are values without any magnification correction. The CIGALE models assume a fixed stellar metallicity value set to  $Z_{\odot}$ , as this code only permits a few discrete values.

$1.5 \pm 0.6 \times 10^{10} M_{\odot}$ , which is a factor of 2.3 times smaller than the PROSPECTOR median stellar mass value of  $3.5^{+1.4}_{-1.4} \times 10^{10} M_{\odot}$ . This increases to a factor of 3.9 smaller for SPT0418B, for which CIGALE yields  $3.4 \pm 0.7 \times 10^9 M_{\odot}$  compared to  $8.2^{+3.6}_{-3.0} \times 10^9 M_{\odot}$  for PROSPECTOR. These differences in the inferred stellar masses are largely driven by the different models for the star formation history: in CIGALE, we assumed a declining exponential SFH with a burst component, with an inferred 80% of the galaxy’s stellar mass formed in the recent burst. The non-parametric SFH model we used in PROSPECTOR does not *a priori* assume a shape for the SFH, rather it fits for the stellar mass formed in each bin and estimates that only 40% of the total galaxy stellar mass was formed in a recent burst, with a significant fraction of the stellar mass having formed at earlier times. We verified that if we require the SFH to be the same in both codes, then the two codes give consistent results.

Setting aside the offset between the two codes for the derived stellar masses, the ratio of the stellar masses for SPT0418A and SPT0418B is consistent between the two codes. Accounting for magnification, the inferred true stellar mass ratios are  $4.5 \pm 1.0$  for CIGALE and  $4.2^{+1.9}_{-1.6}$  for PROSPECTOR, respectively. The uncertainties are large, but still enable us to conclude that this system is consistent with being a  $\sim 4$  to 1 ongoing minor merger between the two galaxies. In this context, the extended structure associated with SPT0418A is potentially a tidal feature arising from the interaction.

It is interesting to consider the effect of this merger upon the stellar populations in these galaxies. Rizzo et al. (2020) found a dynamically well-ordered disk in SPT0418A, which would argue that the interaction has not significantly influenced the internal dynamics. The specific star formation rate (sSFR) of SPT0418A is consistent with estimates for the star-forming main sequence at  $z = 4$  as found in Bouwens et al. (2012) for UV dropout Lyman break galaxies, and similar to what is

seen by da Cunha et al. (2015) for ALESS galaxies. The sSFR of SPT0418A therefore appears to not be significantly elevated by the merger. The specific SFR (sSFR) of SPT0418B is also  $< 10^{-8} \text{ yr}^{-1}$  from both codes, comparable to typical values found for star-forming galaxies at this redshift (see Heinis et al. 2014, and references therein). Interestingly, despite this ongoing collision, there is no evidence that the merger event is actively elevating the star formation in either galaxy.

## 5. CONCLUSIONS

In this paper we use JWST NIRCcam and MIRI imaging of SPT0418–47, which is at a redshift ( $z = 4.225$ ), from the TEMPLATES Early Release Science program to investigate the unlensed properties of the SPT0418–47 system. We analyze the stellar emission from both SPT0418A and the multiply-imaged companion galaxy (SPT0418B), deriving a lensing model and determining stellar masses. [C II] data from ALMA confirms that SPT0418B lies at the same redshift as SPT0418A, which was also reported in Peng et al. (2022), and exhibits a velocity gradient consistent with internal rotation.

From our lensing model reconstruction of the source plane, we determine that the projected physical offset between the centroids of the SPT0418A and SPT0418B. We measure a value of  $4.42 \pm 0.05$  kpc in the source plane, which is broadly consistent with the estimate of Peng et al. (2022). We also see tentatively evidence for extended features associated with SPT0418A. The ALMA data also demonstrate that the mean velocity offset between the two galaxies is  $-56 \text{ km s}^{-1}$ . Fits to the SEDs of both sources using both PROSPECTOR and CIGALE indicate that the stellar mass ratio of the two galaxies is approximately 4 to 1 —  $4.5 \pm 1.0$  for CIGALE and  $4.2^{+1.9}_{-1.6}$  for PROSPECTOR. The simplest interpretation of these results is that we are witnessing an ongoing minor merger in this system. Despite this merger, there is no evidence for elevated sSFRs in either galaxy. Thus,

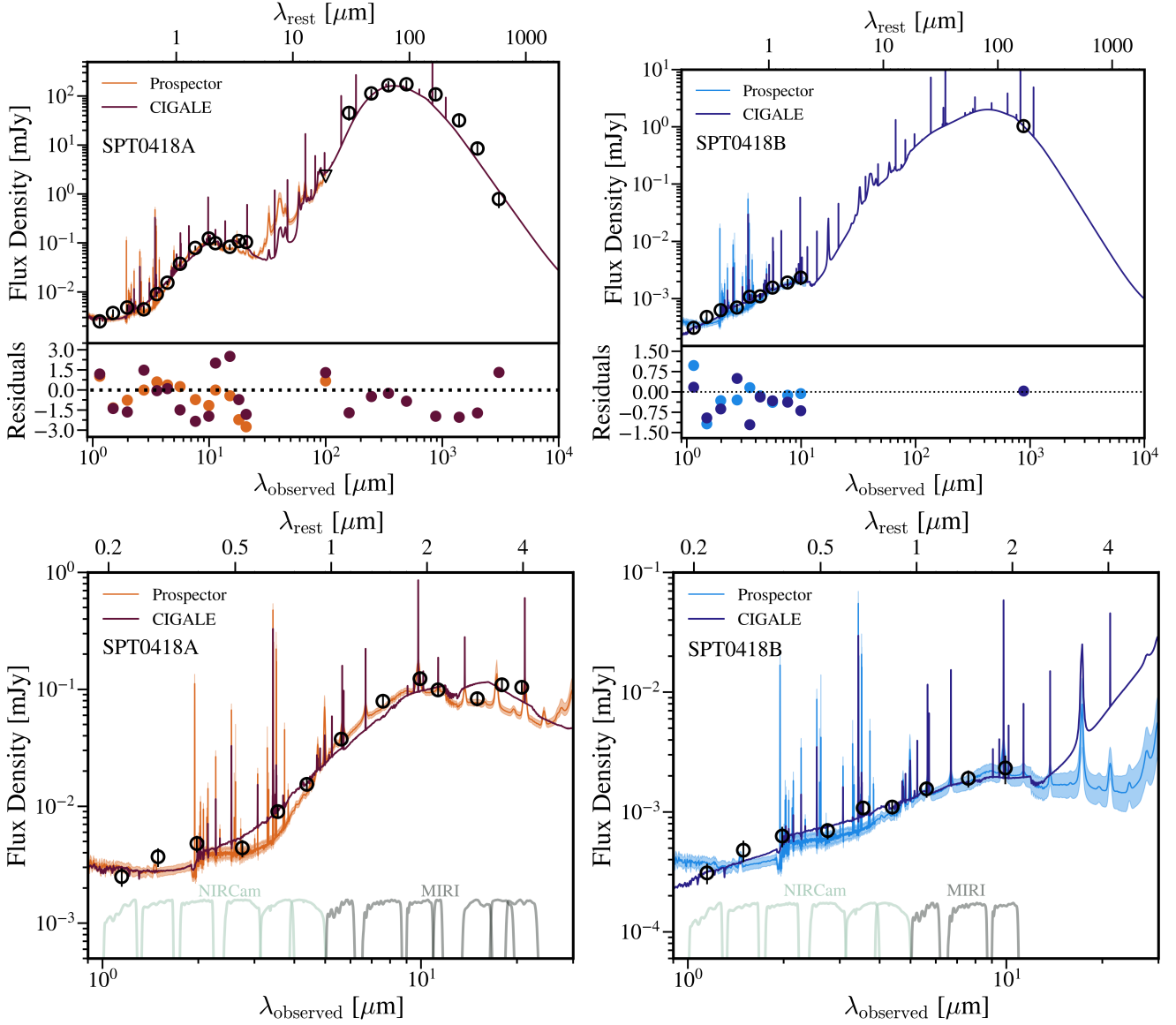


**Figure 7.** Top: UV-FIR Spectral energy distributions (SEDs) for SPT0418A (left) and SPT0418B (right), with observed photometry not corrected for magnification. The best-fit models from PROSPECTOR and CIGALE are shown as shaded bands and solid curves, respectively. The PROSPECTOR SED is the median model SED with the 16<sup>th</sup> – 84<sup>th</sup> percentiles shown in the shaded regions, while the best-fit CIGALE SED is the model corresponding to the minimum  $\chi^2$ . The corresponding model parameters can be found in Table 2. Bottom: Zoom-in to rest-frame UV and optical.

the two galaxies are consistent with the star-formation main sequence at their redshift. After applying the magnification correction, we find that SPT0418A has a stellar mass of  $M_\star = 3.4_{-1.4}^{+1.4} \times 10^{10} M_\odot$  from PROSPECTOR, or  $M_\star = 1.5 \pm 0.6 \times 10^{10} M_\odot$  from CIGALE, and SPT0418B has a stellar mass of  $M_\star = 8.2_{-3.0}^{+3.6} \times 10^9 M_\odot$  from PROSPECTOR, or  $M_\star = 3.4 \pm 0.7 \times 10^9 M_\odot$  from CIGALE. We suggest that the difference between these two codes is due to different star assumed formation histories found by each.

Finally, we have compared the results of fitting the SEDs with PROSPECTOR and CIGALE. The two codes

yield similar SFRs, effective extinctions (Table 2), and stellar mass ratios. PROSPECTOR however yields stellar masses that are systematically higher by factors of  $\sim 2$ – $4$ . This difference, which is largely driven by differences in the models of the star formation history, highlights that caution should be exercised when comparing stellar mass estimates in the literature that use different codes and input assumptions (see also Michałowski et al. 2014; Mobasher et al. 2015; Hunt et al. 2019).

## 6. ACKNOWLEDGMENTS

This work is based in part on observations made with the NASA/ESA/CSA JWST. The data were obtained from the Mikulski Archive for Space Telescopes at the Space Telescope Science Institute, which is operated by the Association of Universities for Research in Astronomy, Inc., under NASA contract NAS 5-03127 for JWST. These observations are associated with ERS program #1355. We express our gratitude to the thousands of people around the world who brought to fruition JWST and its science instruments NIRCam and MIRI.

The SPT is supported by the NSF through grant OPP-1852617. This paper makes use of the following ALMA data: ADS/NSF.ALMA#2016.1.01374.S and #2016.1.01499.S ALMA is a partnership of ESO (representing its member states), NSF (USA) and NINS (Japan), together with NRC (Canada), MOST and ASIAA (Taiwan), and KASI (Republic of Korea), in cooperation with the Republic of Chile. The Joint ALMA Observatory is operated by ESO, AUI/NRAO and NAOJ. The National Radio Astronomy Observatory is a facility of the National Science Foundation operated

under cooperative agreement by Associated Universities, Inc.

Support for this program was provided by NASA through a grant from the Space Telescope Science Institute (JWST-ERS-01355), which is operated by the Association of Universities for Research in Astronomy, Inc., under NASA contract NAS 5-03127. M.A. acknowledges support from FONDECYT grant 1211951 and CONICYT + PCI + INSTITUTO MAX PLANCK DE ASTRONOMIA MPG190030. D.P.M. J.D.V., and K.P. acknowledge support from the US NSF under grants AST-1715213 and AST-1716127. MA and MS acknowledge support from and CONICYT + PCI + REDES 190194, and ANID BASAL project FB210003. D.N. was supported by the NSF via AST-1909153. K.A.P. is supported by the Center for AstroPhysical Surveys at the National Center for Supercomputing Applications as an Illinois Survey Science Graduate Fellow. N.S. is a member of the International Max Planck Research School (IMPRS) for Astronomy and Astrophysics at the Universities of Bonn and Cologne.

## APPENDIX

### A. PHOTOMETRY

We present the photometric data used in modeling the SEDs in Figure 7. Table 3 includes the JWST photometry from NIRCam and MIRI, while Table 4 summarizes the longer wavelength literature fluxes from Reuter et al. (2020). The values in Table 4 correspond to the total flux from SPT0418A and SPT0418B. As discussed in the text, when fitting the SEDs for the two components we assign  $95.8 \pm 2.2\%$  of the flux in the FIR bands to SPT0418A. This percentage corresponds to the fraction of the flux associated with SPT0418A in the ALMA imaging, and we assume the same fractional contribution for the other FIR observations.

## REFERENCES

- Alaghband-Zadeh, S., Chapman, S. C., Swinbank, A. M., et al. 2012, MNRAS, 424, 2232, doi: [10.1111/j.1365-2966.2012.21386.x](https://doi.org/10.1111/j.1365-2966.2012.21386.x)
- Baugh, C. M., Cole, S., & Frenk, C. S. 1996, MNRAS, 283, 1361, doi: [10.1093/mnras/283.4.1361](https://doi.org/10.1093/mnras/283.4.1361)
- Birrer, S., & Amara, A. 2018, Physics of the Dark Universe, 22, 189, doi: [10.1016/j.dark.2018.11.002](https://doi.org/10.1016/j.dark.2018.11.002)
- Birrer, S., Amara, A., & Refregier, A. 2015, The Astrophysical Journal, 813, 102, doi: [10.1088/0004-637x/813/2/102](https://doi.org/10.1088/0004-637x/813/2/102)
- Birrer, S., Shajib, A., Gilman, D., et al. 2021, Journal of Open Source Software, 6, 3283, doi: [10.21105/joss.03283](https://doi.org/10.21105/joss.03283)
- Boquien, M., Burgarella, D., Roehly, Y., et al. 2019, A&A, 622, A103, doi: [10.1051/0004-6361/201834156](https://doi.org/10.1051/0004-6361/201834156)
- Bouwens, R. J., Illingworth, G. D., Oesch, P. A., et al. 2012, ApJ, 754, 83, doi: [10.1088/0004-637X/754/2/83](https://doi.org/10.1088/0004-637X/754/2/83)
- Boyer, M. L., Anderson, J., Gennaro, M., et al. 2022, Research Notes of the American Astronomical Society, 6, 191, doi: [10.3847/2515-5172/ac923a](https://doi.org/10.3847/2515-5172/ac923a)
- Bruzual, G., & Charlot, S. 2003, MNRAS, 344, 1000, doi: [10.1046/j.1365-8711.2003.06897.x](https://doi.org/10.1046/j.1365-8711.2003.06897.x)
- Chabrier, G. 2003, PASP, 115, 763, doi: [10.1086/376392](https://doi.org/10.1086/376392)
- Conroy, C., & Gunn, J. E. 2010, The Astrophysical Journal, 712, 833–857, doi: [10.1088/0004-637x/712/2/833](https://doi.org/10.1088/0004-637x/712/2/833)
- Conroy, C., Gunn, J. E., & White, M. 2009, The Astrophysical Journal, 699, 486–506, doi: [10.1088/0004-637x/699/1/486](https://doi.org/10.1088/0004-637x/699/1/486)

**Table 3.** NIRCam and MIRI Data

Filter	$\lambda^a$ $\mu\text{m}$	$\Delta\lambda$ $\mu\text{m}$	Int. Time (s)	SPT 0418A ( $\mu\text{Jy}$ )	SPT 0418B ( $\mu\text{Jy}$ )
F115W	1.154	0.225	687	2.5 $\pm$ 0.2	0.31 $\pm$ 0.03
F150W	1.501	0.318	343	3.7 $\pm$ 0.3	0.48 $\pm$ 0.05
F200W	1.990	0.461	429	4.8 $\pm$ 0.3	0.63 $\pm$ 0.06
F277W	2.786	0.672	687	4.4 $\pm$ 0.3	0.70 $\pm$ 0.04
F356W	3.563	0.787	343	9.0 $\pm$ 0.2	1.08 $\pm$ 0.03
F444W	4.421	1.024	429	15.4 $\pm$ 0.2	1.10 $\pm$ 0.04
F560W	5.6	1.2	277	37.5 $\pm$ 0.5	1.56 $\pm$ 0.09
F770W	7.7	2.2	144	79.1 $\pm$ 0.9	1.91 $\pm$ 0.12
F1000W	10	2.0	111	123.3 $\pm$ 2.2	2.33 $\pm$ 0.39
F1280W	12.8	2.4	111	98.9 $\pm$ 1.4	...
F1500W	15	3.0	111	83.1 $\pm$ 3.3	...
F1800W	18	3.0	222	109.3 $\pm$ 3.6	...
F2100W	22	5.0	832	104.1 $\pm$ 3.4	...

<sup>a</sup>For NIRCam  $\lambda$  refers to the pivot wavelength, while for MIRI  $\lambda$  is simply the central wavelength.

NOTE—Quoted flux densities are observed values without any magnification correction. The fluxes for the SPT0418B are for the outer image alone. See §4.2 for more details on the photometry measurements.

**Table 4.** Published SPT0418–47 FIR Photometry from Reuter et al. (2020)

$\lambda$ ( $\mu\text{m}$ )	Flux Density (mJy)
100	< 7
160	45 $\pm$ 8
250	114 $\pm$ 6
350	166 $\pm$ 6
500	175 $\pm$ 7
870	108 $\pm$ 11
1400	32 $\pm$ 5
2000	9 $\pm$ 1
3000	0.79 $\pm$ 0.14

da Cunha, E., Walter, F., Smail, I. R., et al. 2015, ApJ, 806, 110, doi: [10.1088/0004-637X/806/1/110](https://doi.org/10.1088/0004-637X/806/1/110)

De Breuck, C., Weiß, A., Béthermin, M., et al. 2019, A&A, 631, A167, doi: [10.1051/0004-6361/201936169](https://doi.org/10.1051/0004-6361/201936169)

Engel, H., Tacconi, L. J., Davies, R. I., et al. 2010, ApJ, 724, 233, doi: [10.1088/0004-637X/724/1/233](https://doi.org/10.1088/0004-637X/724/1/233)

Foreman-Mackey, D., Hogg, D. W., Lang, D., & Goodman, J. 2013, PASP, 125, 306, doi: [10.1086/670067](https://doi.org/10.1086/670067)

Governato, F., Brook, C. B., Brooks, A. M., et al. 2009, MNRAS, 398, 312, doi: [10.1111/j.1365-2966.2009.15143.x](https://doi.org/10.1111/j.1365-2966.2009.15143.x)

Heinis, S., Buat, V., Béthermin, M., et al. 2014, MNRAS, 437, 1268, doi: [10.1093/mnras/stt1960](https://doi.org/10.1093/mnras/stt1960)

- Hopkins, P. F., Hernquist, L., Cox, T. J., & Kereš, D. 2008, *ApJS*, 175, 356, doi: [10.1086/524362](https://doi.org/10.1086/524362)
- Hopkins, P. F., Bundy, K., Croton, D., et al. 2010, *ApJ*, 715, 202, doi: [10.1088/0004-637X/715/1/202](https://doi.org/10.1088/0004-637X/715/1/202)
- Hunt, L. K., De Looze, I., Boquien, M., et al. 2019, *A&A*, 621, A51, doi: [10.1051/0004-6361/201834212](https://doi.org/10.1051/0004-6361/201834212)
- Johnson, B. D., Leja, J., Conroy, C., & Speagle, J. S. 2021, *ApJS*, 254, 22, doi: [10.3847/1538-4365/abef67](https://doi.org/10.3847/1538-4365/abef67)
- Kennedy, J., & Eberhart, R. 1995, in *Proceedings of ICNN'95 - International Conference on Neural Networks*, Vol. 4, 1942–1948 vol.4, doi: [10.1109/ICNN.1995.488968](https://doi.org/10.1109/ICNN.1995.488968)
- Kriek, M., & Conroy, C. 2013, *ApJL*, 775, L16, doi: [10.1088/2041-8205/775/1/L16](https://doi.org/10.1088/2041-8205/775/1/L16)
- Leja, J., Carnall, A. C., Johnson, B. D., Conroy, C., & Speagle, J. S. 2019, *ApJ*, 876, 3, doi: [10.3847/1538-4357/ab133c](https://doi.org/10.3847/1538-4357/ab133c)
- Litke, K. C., Marrone, D. P., Spilker, J. S., et al. 2019, *ApJ*, 870, 80, doi: [10.3847/1538-4357/aaf057](https://doi.org/10.3847/1538-4357/aaf057)
- Lower, S., Narayanan, D., Leja, J., et al. 2020, *ApJ*, 904, 33, doi: [10.3847/1538-4357/abbfa7](https://doi.org/10.3847/1538-4357/abbfa7)
- . 2022, *ApJ*, 931, 14, doi: [10.3847/1538-4357/ac6959](https://doi.org/10.3847/1538-4357/ac6959)
- Marrone, D. P., Spilker, J. S., Hayward, C. C., et al. 2018, *Nature*, 553, 51, doi: [10.1038/nature24629](https://doi.org/10.1038/nature24629)
- Massey, R., & Refregier, A. 2005, *Monthly Notices of the Royal Astronomical Society*, 363, 197, doi: [10.1111/j.1365-2966.2005.09453.x](https://doi.org/10.1111/j.1365-2966.2005.09453.x)
- McElwain, M. W., Feinberg, L. D., Perrin, M. D., et al. 2023, *PASP*, 135, 058001, doi: [10.1088/1538-3873/acada0](https://doi.org/10.1088/1538-3873/acada0)
- McMullin, J. P., Waters, B., Schiebel, D., Young, W., & Golap, K. 2007, in *Astronomical Society of the Pacific Conference Series*, Vol. 376, *Astronomical Data Analysis Software and Systems XVI*, ed. R. A. Shaw, F. Hill, & D. J. Bell, 127
- Michałowski, M. J., Hayward, C. C., Dunlop, J. S., et al. 2014, *A&A*, 571, A75, doi: [10.1051/0004-6361/201424174](https://doi.org/10.1051/0004-6361/201424174)
- Mobasher, B., Dahlen, T., Ferguson, H. C., et al. 2015, *ApJ*, 808, 101, doi: [10.1088/0004-637X/808/1/101](https://doi.org/10.1088/0004-637X/808/1/101)
- Nelson, E. J., Suess, K. A., Bezanson, R., et al. 2022, *arXiv e-prints*, arXiv:2208.01630, doi: [10.48550/arXiv.2208.01630](https://doi.org/10.48550/arXiv.2208.01630)
- Peng, B., Vishwas, A., Stacey, G., et al. 2022, *arXiv e-prints*, arXiv:2210.16968, <https://arxiv.org/abs/2210.16968>
- Peng, C. Y., Ho, L. C., Impey, C. D., & Rix, H.-W. 2002, *AJ*, 124, 266, doi: [10.1086/340952](https://doi.org/10.1086/340952)
- . 2010, *AJ*, 139, 2097, doi: [10.1088/0004-6256/139/6/2097](https://doi.org/10.1088/0004-6256/139/6/2097)
- Perrin, M. D., Sivaramakrishnan, A., Lajoie, C.-P., et al. 2014, in *Society of Photo-Optical Instrumentation Engineers (SPIE) Conference Series*, Vol. 9143, *Space Telescopes and Instrumentation 2014: Optical, Infrared, and Millimeter Wave*, ed. J. Oschmann, Jacobus M., M. Clampin, G. G. Fazio, & H. A. MacEwen, 91433X, doi: [10.1117/12.2056689](https://doi.org/10.1117/12.2056689)
- Perrin, M. D., Soummer, R., Elliott, E. M., Lallo, M. D., & Sivaramakrishnan, A. 2012, in *Society of Photo-Optical Instrumentation Engineers (SPIE) Conference Series*, Vol. 8442, *Space Telescopes and Instrumentation 2012: Optical, Infrared, and Millimeter Wave*, ed. M. C. Clampin, G. G. Fazio, H. A. MacEwen, & J. Oschmann, Jacobus M., 84423D, doi: [10.1117/12.925230](https://doi.org/10.1117/12.925230)
- Perry, R. W., Chapman, S. C., Smail, I., & Bertoldi, F. 2022, *arXiv e-prints*, arXiv:2210.08191, doi: [10.48550/arXiv.2210.08191](https://doi.org/10.48550/arXiv.2210.08191)
- Pillepich, A., Nelson, D., Springel, V., et al. 2019, *MNRAS*, 490, 3196, doi: [10.1093/mnras/stz2338](https://doi.org/10.1093/mnras/stz2338)
- Planck Collaboration, Aghanim, N., Akrami, Y., et al. 2020, *A&A*, 641, A6, doi: [10.1051/0004-6361/201833910](https://doi.org/10.1051/0004-6361/201833910)
- Refregier, A. 2003, *Monthly Notices of the Royal Astronomical Society*, 338, 35, doi: [10.1046/j.1365-8711.2003.05901.x](https://doi.org/10.1046/j.1365-8711.2003.05901.x)
- Refregier, A., & Bacon, D. 2003, *Monthly Notices of the Royal Astronomical Society*, 338, 48, doi: [10.1046/j.1365-8711.2003.05902.x](https://doi.org/10.1046/j.1365-8711.2003.05902.x)
- Reuter, C., Vieira, J. D., Spilker, J. S., et al. 2020, *ApJ*, 902, 78, doi: [10.3847/1538-4357/abb599](https://doi.org/10.3847/1538-4357/abb599)
- Rigby, J., Perrin, M., McElwain, M., et al. 2023, *Publications of the Astronomical Society of the Pacific*, 135, 048001, doi: [10.1088/1538-3873/acb293](https://doi.org/10.1088/1538-3873/acb293)
- Rizzo, F., Vegetti, S., Powell, D., et al. 2020, *Nature*, 584, 201, doi: [10.1038/s41586-020-2572-6](https://doi.org/10.1038/s41586-020-2572-6)
- Robertson, B., Bullock, J. S., Cox, T. J., et al. 2006, *ApJ*, 645, 986, doi: [10.1086/504412](https://doi.org/10.1086/504412)
- Roman-Oliveira, F., Fraternali, F., & Rizzo, F. 2023, *arXiv e-prints*, arXiv:2302.03049, doi: [10.48550/arXiv.2302.03049](https://doi.org/10.48550/arXiv.2302.03049)
- Sanders, D. B., Soifer, B. T., Elias, J. H., et al. 1988, *ApJ*, 325, 74, doi: [10.1086/165983](https://doi.org/10.1086/165983)
- Sotillo-Ramos, D., Pillepich, A., Donnari, M., et al. 2022, *MNRAS*, 516, 5404, doi: [10.1093/mnras/stac2586](https://doi.org/10.1093/mnras/stac2586)
- Spilker, J. S., Aravena, M., Phadke, K. A., et al. 2020, *ApJ*, 905, 86, doi: [10.3847/1538-4357/abc4e6](https://doi.org/10.3847/1538-4357/abc4e6)
- Steinmetz, M., & Navarro, J. F. 2002, *NewA*, 7, 155, doi: [10.1016/S1384-1076\(02\)00102-1](https://doi.org/10.1016/S1384-1076(02)00102-1)
- THE CASA TEAM, Bean, B., Bhatnagar, S., et al. 2022, *arXiv e-prints*, arXiv:2210.02276, <https://arxiv.org/abs/2210.02276>

Vieira, J. D., Marrone, D. P., Chapman, S. C., et al. 2013,  
Nature, 495, 344, doi: [10.1038/nature12001](https://doi.org/10.1038/nature12001)